ADVANCES IN ATMOSPHERIC SCIENCES, VOL. 39, DECEMBER 2022, 2040–2055

• **Original Paper** •

Macro- and Micro-physical Characteristics of Different Parts of Mixed Convective-stratiform Clouds and Differences in Their Responses to Seeding※

Dejun LI[1], Chuanfeng ZHAO*[2], Peiren LI[3], Cao Liu[4], Dianli GONG[5], Siyao LIU[2], Zhengteng YUAN[1], and Yingying CHEN[1]

[1]*Hubei Meteorological Service Center*, *Wuhan* 430205, *China*

[2]*College of Global Change and Earth System Science*, *Beijing Normal University*, *Beijing* 100875, *China*

[3]*Weather Modification Office of Shanxi Province*, *Taiyuan* 030032, *China*

[4]*Wuhan Central Meteorological Observatory*, *Wuhan* 430074, *China*

[5]*Weather Modification Office of Shandong Province*, *Jinan* 250031, *China*

(Received 13 January 2022; revised 25 April 2022; accepted 11 May 2022)

ABSTRACT

This study investigates the cloud macro- and micro-physical characteristics in the convective and stratiform regions and their different responses to the seeding for mixed convective-stratiform clouds that occurred in Shandong province on 21 May 2018, based on the observations from the aircraft, the Suomi National Polar-Orbiting Partnership (NPP) satellite, and the high-resolution Himawari-8 (H8) satellite. The aircraft observations show that convection was deeper and radar echoes were significantly enhanced with higher tops in response to seeding in the convective region. This is linked with the conversion of supercooled liquid droplets to ice crystals with released latent heat, resulting in strengthened updrafts, enhanced radar echoes, higher cloud tops, and more and larger precipitation particles. In contrast, in the stratiform cloud region, after the Silver Iodide (AgI) seeding, the radar echoes become significantly weaker at heights close to the seeding layer, with the echo tops lowered by 1.4–1.7 km. In addition, a hollow structure appears at the height of 6.2–7.8 km with a depth of about 1.6 km and a diameter of about 5.5 km, and features such as icing seeding tracks appear. These suggest that the transformation between droplets and ice particles was accelerated by the seeding in the stratiform part. The NPP and H8 satellites also show that convective activity was stronger in the convective region after seeding; while in the stratiform region, a cloud seeding track with a width of 1–3 km appears 10 km downstream of the seeding layer 15 minutes after the AgI seeding, which moves along the wind direction as width increases.

Key words: airborne Ka-band Precipitation Radar (KPR), mixed convective-stratiform clouds, convective region, stratiform region, cloud seeding, cloud microphysical properties

Citation: Li, D. J., C. F. Zhao, P. R. Li, C. Liu, D. L. Gong, S. Y. Liu, Z. T. Yuan, and Y. Y. Chen, 2022: Macro- and micro-physical characteristics of different parts of mixed convective-stratiform clouds and differences in their responses to seeding. *Adv. Atmos. Sci.*, **39**(12), 2040−2055, https://doi.org/10.1007/s00376-022-2003-8.

Article Highlights:

- Enhanced convective activity occurs with higher cloud tops in response to seeding in convective cloud regions.
- Dynamic seeding mechanism is involved in the convective cloud region, resulting in more and larger precipitation particles.
- Conversion of liquid to ice particles is accelerated with weaker radar echoes around the seeding layer in the stratiform cloud region.

1. Introduction

Water is critical to human society and the natural environment. As water resources are limited, the continuously-increasing human demands have prompted considerable interest in the feasibility of increasing water supply through weather modification. To increase the precipitation, espe-

※ This paper is a contribution to the special issue on Cloud–Aerosol–Radiation–Precipitation Interaction: Progress and Challenges.

* Corresponding author: Chuanfeng ZHAO
Email: czhao@bnu.edu.cn

cially for arid and semi-arid regions, cold-cloud seeding experiments have been conducted since the 1940s (Smith, 1949; Langmuir, 1950; Vonnegut and Chessin, 1971; Hobbs et al., 1981; Bruintjes, 1999; Dong et al., 2020). Because the Silver Iodide (AgI) has similar crystal structure to ice (Vonnegut and Chessin, 1971), its particles can act as ice nuclei (IN) (DeMott, 1997). Thus, AgI has been widely used in cloud seeding both from the ground and in the air. Seeding with AgI can increase both precipitation and snowfall, thus changing the equilibrium between the water supply and demand (Xue et al., 2013a, b, 2014; Boe et al., 2014; Jing and Geerts, 2015; Jing et al., 2015, 2016).

Since the beginning of weather modification, numerous studies have been conducted on the effects of cloud seeding experiments on the precipitation and cloud microphysical characteristics over target areas (Biondini et al., 1977; Nirel and Rosenfeld, 1995; Gabriel, 1999; Silverman, 2001; Woodley et al., 2003; Woodley and Rosenfeld, 2004; Pokharel et al., 2015). In recent years, with the application of airborne detection equipment, the cloud microphysical characteristics (Lawson et al., 2006, 2008, 2019; Yang et al., 2019; Zhao et al., 2019) and variation in cloud responses to seeding (Heymsfield et al., 2011; Cai et al., 2013; Dong et al., 2020) can be more accurately analyzed. By using the Advanced Very High Resolution Radiometer (AVHRR) onboard the National Oceanic and Atmospheric Administration (NOAA) polar orbiting satellites, Rosenfeld et al. (2005) observed a cloud seeding track formed after seeding, with a duration of 38 minutes. Using a ground-based X-band radar, airborne W-band cloud radar, and other aircraft instruments, French et al. (2018) observed the process that the cloud seeding with AgI in supercooled stratus causes the transformation of surrounding supercooled water into ice crystals, followed by the deposition of water vapor and the growth of ice crystals.

The studies mentioned above demonstrate that static seeding can play a significant role (Bruintjes, 1999). In the presence of humid, neutral or unstable atmospheric conditions, the release of latent heat due to the ice formation in clouds causes nearby air to gain buoyancy and further changes the flow field, resulting in deeper convective clouds, which is known as the dynamic seeding mechanism (Simpson and Woodley, 1971; Rosenfeld et al., 1989). Scientists have studied the dynamic seeding mechanism with experiments mainly for summer convection (from cumulus to cumulonimbus clouds). However, due to the limitation of detection methods and the factors such as rapid formation and dissipation of convective clouds, it is challenging to trace the changes in macro- and microphysical characteristics caused by the seeding of catalysts. Hence, researchers have focused mostly on the changes of cloud-top height and surface precipitation but not on the detailed physical processes. Therefore, the dynamic seeding mechanism still lacks the verification through directly-observed data (Sax et al., 1979; Hallet, 1981; Woodley et al., 1982; Orville, 1996). Due to the complex structural characteristics of mixed convective-stratiform clouds (Lawson et al., 2015; Lin et al., 2019), there have been few studies related to the response of different cloud parts after seeding, such as the convective and stratiform parts, as well as the presence or absence of dynamic seeding effects.

In 2014, the University of Wyoming developed the airborne Ka-band precipitation cloud radar (KPR), which is well known for its high spatio-temporal resolution with 0.1–20 μs sampling time resolution and 30 m spatial resolution. This radar provides direct observation of cloud property responses to seeding in the context of both macro- and microphysical characteristics (Heymsfield et al., 2013; Pazmany and Haimov, 2018). In addition, the Suomi National Polar-Orbiting Partnership (NPP) satellite in 2011 and the Himawari-8 (H8) satellite in 2014 were successfully launched successively, and the resolution of thermal infrared bands of the NPP/ VIIRS (Visible Infrared Imaging Radiometer Suite Sensor) has been improved by a factor of 3 compared with sensors such as the Moderate Resolution Imaging Spectroradiometer (MODIS), providing unique advantages in accurately resolving small convective clouds during their initial/developing stages, and also in monitoring the cloud track (Hillger et al., 2013; Rosenfeld et al., 2014). In this study, to the best of our knowledge, for the first time in China we used the airborne KPR to monitor the evolving characteristics of radar echoes before and after the seeding for a spring mixed convective-stratiform cloud. The target was such a cloud that occurred in Shandong Province on 21 May 2018. Moreover, we combined the satellite observations and other data to comprehensively analyze the cloud characteristics in the stratiform region and the role of possible dynamic seeding mechanism in the convective region.

The remainder of this paper is organized as follows. The data sources used are introduced in section 2. Section 3 presents the synoptic situation and experiment overview. Section 4 shows the main results of this study. A conceptual model of seeding in different parts of mixed convective-stratiform clouds is proposed in section 5. Finally, the conclusions and discussion are given in section 6.

2. Data

The data used in this study are obtained from aircraft, satellite and ground observations. The experiment area for cloud detection and seeding was the region bounded by 117°–119°E, 36.5°–37.5°N. The ground observations include the synoptic meteorological observation data in Shandong Province and 6-mminute S-band Doppler weather radar data from Binzhou in Shandong on 21 May 2018. Here, the airborne data and satellite data are described.

2.1. *Airborne data*

The King Air aircraft was used for the cloud seeding and making observations. This aircraft is owned by the Shanxi Victory General Aviation Co., LTD and operated by the Shandong Province Weather Modification Office. The aircraft was equipped with instruments for measuring the

cloud, precipitation and other meteorological elements, including the airborne KPR, the particle size probes from Droplet Measurement Technologies (DMT) and 20 Hz Aircraft-Integrated Meteorological Measurement System (AIMMS-20). It was also equipped with the Beidou satellite navigation and position system and a flare rack with positions for 24 flares, as shown in Fig. 1. The airborne KPR (ProSensing, USA) is the Ka-band precipitation cloud radar, which scans vertically, both upward and downward, and employs a data processing technique using the coherent power spectrum to reduce the noise. The Cloud Droplet Probe (CDP, DMT) based on forward-scattering theory, has 30 size bins, with a sampling frequency of 1 Hz, and a measurement range of 2–50 μm with a resolution of 1–2 μm. It can measure particle number concentrations in the range of 0–1.0×10^4 cm^{-3}, with the uncertainty of approximately 20% (Lance, 2012; Yang et al, 2019, 2020). The Cloud Imaging Probe (CIP, DMT) has 62 size bins, with a sampling frequency of 1 Hz, a measurement range of 25–1550 μm and a resolution of 25 μm. The Precipitation Imaging Probe (PIP, DMT) has the same number of size bins and sampling frequency as the CIP. However, the PIP has a measurement range of 100–6200 μm with a bin width of 100 μm. The specifications for the main instruments used in this study are listed in Table 1, including the measurement ranges, temporal resolution and the particle size spectral bin resolution. Note that both cloud and precipitation particle probes are calibrated in the ground laboratory before every flight.

2.2. *Satellite data*

The NPP VIIRS satellite observations at 0525 UTC on 21 May 2018 were used in this study, which is provided to the public by NOAA (http://www.bou.class.noaa.gov/saa/products/welcome). It has five channels with central wavelengths at 0.64, 0.865, 1.615, 3.745 and 11.45 μm, with high spatial resolution of 375 m. During the passage of the NPP satellite by the study region at 0525 UTC on 21 May 2018, the time past the aircraft seeding and detection activities at

Fig. 1. Photos of the King Air aircraft probes, including AgI flares equipment, Ka-band cloud radar (KPR), cloud combination probe (CCP), cloud imaging probe (CIP), precipitation image probe (PIP), 20 Hz Aircraft-Integrated Meteorological Measurement System (AIMMS-20), Passive Cavity Aerosol Spectrometer Probe (PCASP), cloud condensation nuclei (CCN) counter and Hot-Wire Liquid Water Content Sensor (LWC-100).

Table 1. The main instruments and their detection variables used in this study, along with the measurement ranges, spatio-temporal resolution and the particle size spectral bin resolution.

Instrument	Variables detected	Measurement range	Resolution
Airborne Ka-band Radar (KPR)	Reflectivity	−25–55 dBZ	Spatial: 30 m;
	Radial velocity	−21–21 m s^{-1}	Time: 0.2 s
CDP	Droplet size distribution	2–50 μm	1 μm
CIP	Cloud particle image	25–1550 μm	25 μm
PIP	Precipitation particle image	100–6200 μm	100 μm
AIMMS-20	Meteorology (temperature, humidity, and wind)	–	–

A–B–C–D–E–F–G is about 33–28–27–16–15–6–6 minutes.

The 10-minute full-disc data from the H8 on 21 May provided by the Data Service (http://www.bou.class.noaa.gov/saa/products/welcome) were also used in this study. The Advanced Himawari Imager (AHI, ftp://ftp.ptree.jaxa.jp) onboard the H8 completes each full-disc scan within 10 minutes, greatly facilitating the tracking of the developing cloud seeding tracks. The H8/AHI sensor has 16 channels ranging from 0.46 to 13.3 μm. Meanwhile, the spatial resolution of visible and near-infrared channels ranges from 0.5–1 km, and the spatial resolution of infrared channel is only 2 km.

3. Synoptic situation and experiment overview

3.1. *Synoptic situation*

Figure 2 shows that Shandong was dominated by westerly flow at 700 hPa at 0000 UTC on 21 May 2018. There were two weak waves in the westerlies successively advancing eastward that affected Shandong. At 700 hPa, there was a shear with wind direction changing from southwest to southeast around Shandong in the morning, causing more humid air to enter this region and therefore leading to potential more precipitation. Meanwhile, a significant wind shear with wind direction changing from northwest to southwest near the Hetao region moved eastward and continued to affect Shandong, with the wind direction of 300° and wind speed of 11 m s^{-1}, contributing to the precipitation observed in Shandong in the afternoon of the 21st. At the surface, Shandong was located along the western side of the anticyclone circulation over the sea during 0000–1200 UTC on 21 May, dominated by the easterly wind. There was a surface convergence line near the flight track at that time, and the accumulated rainfall at regions near the flight track was 1–7 mm during 0300–0600 UTC.

3.2. *Overview of the seeding and detection experiment*

The flight track over north-central Shandong Province was close to the northern edge of central Taishan Mountains (Fig. 3a). The flight altitude was 5300 m, the flight speed was 101–113 m s^{-1}, and the height of the freezing level was 4200 m. At 0437 UTC, the aircraft was flying at the height of 1800 m over point O1, and the KPR began to make observations. At 0445 UTC, the aircraft circled over point O2 and ascended to 5300 m. During 0452–0519 UTC, the aircraft performed the seeding operation along the zigzag path A–B–C–D–E–F–G. At 0452 UTC, two AgI flares were burned and released at 5300 m (one on each side) simultaneously at point A, and a total of four flares (2 on each side) were burned before 0500 UTC. Note that the burning duration for every flare is 5 minutes. Each flare consists of 27 g AgI, and the nucleation rate of AgI is 1.08×10^{15} per gram at −10°C. The AgI in each flare can effectively play the role of ice nucleus at temperatures below −4°C. At 0500 UTC, within the clouds with sufficient supercooled water (abundant supercooled water particularly within the convective core part about 1–2 km below the aircraft), the aircraft burned a total of eight AgI flares also at 5300 m (4 on each side) with two AgI flares (one on each side) burned simultaneously at a given time. The aircraft finished the seeding operation at point G at 0519 UTC. Note the short overlap time existed between two adjacent flares, which could introduce some uncertainties to the quantitative response of cloud properties to seeding. Afterwards, it descended gradually from 5300 m to point I (2800 m) to conduct a backward detection experiment for the seeding effect. The seeding was carried out along three lines of the zigzag flight track (A–G), with a seeding duration of 27 minutes and a seeding rate of 0.6 g s^{-1}, consuming 972 g AgI (36 flares of 27 g AgI each). Note that different total amounts of AgI flares were released sometimes at two parts of clouds although the released AgI amount at a given time is roughly similar; this could affect the response of clouds to the seeding and make the quantitative comparison

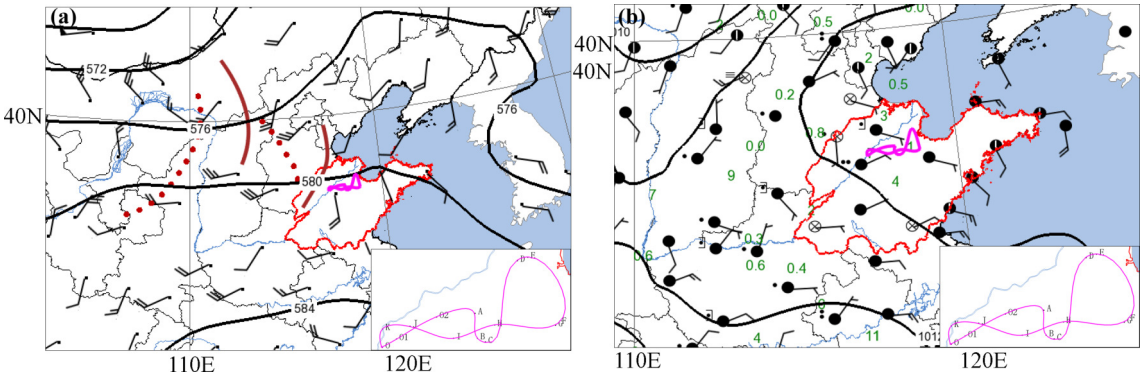

Fig. 2. Synoptic weather situation along with the surface meteorological observations on 21 May 2018. (a) Geopotential height at 500 hPa and the wind at 700 hPa at 0000 UTC, with the thick purple lines representing the weak waves and red dotted lines representing warm/cold shear lines. (b) Surface map depicting weather conditions using the standard synoptic symbols and rainfall at 0600 UTC. The turning points of the seeding track are denoted by the characters O–A–K, and O points marks Jinan Yaoqiang Airport. The seeding area was carried out along the magenta lines of the zigzagging flight track (A–G), and the other magenta lines (O–A and G–O) were the detection area. More clear demonstrations about these flight track points can be seen in Figures 3a, 9 and 10h.

of cloud seeding effect at two locations challenging. To minimize this impact, we mainly analyzed the differences in cloud seeding effect at two locations qualitatively while some quantitative results about the changes of cloud microphysical properties were also provided.

The aircraft returned to point O at 0548 UTC. To compare and analyze the situation before the seeding and the backward detection results in detail, S1–S3 (0454:30–0455:30 UTC) and S4–S6 (0501:22–0502:22 UTC) are marked in Fig. 3a as the two periods of AgI seeding. The middle points of the two seeding periods are marked as S2 and S5, respectively. The time nodes of the backward detection were determined based on the wind direction and speed at the seeding layer. The purple dashed line is the line segment between S2 and S5 moving at 11 m s^{-1} along the wind direction of 300°. It intersects with the line segment G–H of the backward detection, with the crossover points marked as R5 and R2, respectively. Taking the two points R5 and R2 as middle points, respectively, the corresponding backward detection periods are determined as R4–R6 (0526:25–0527:25

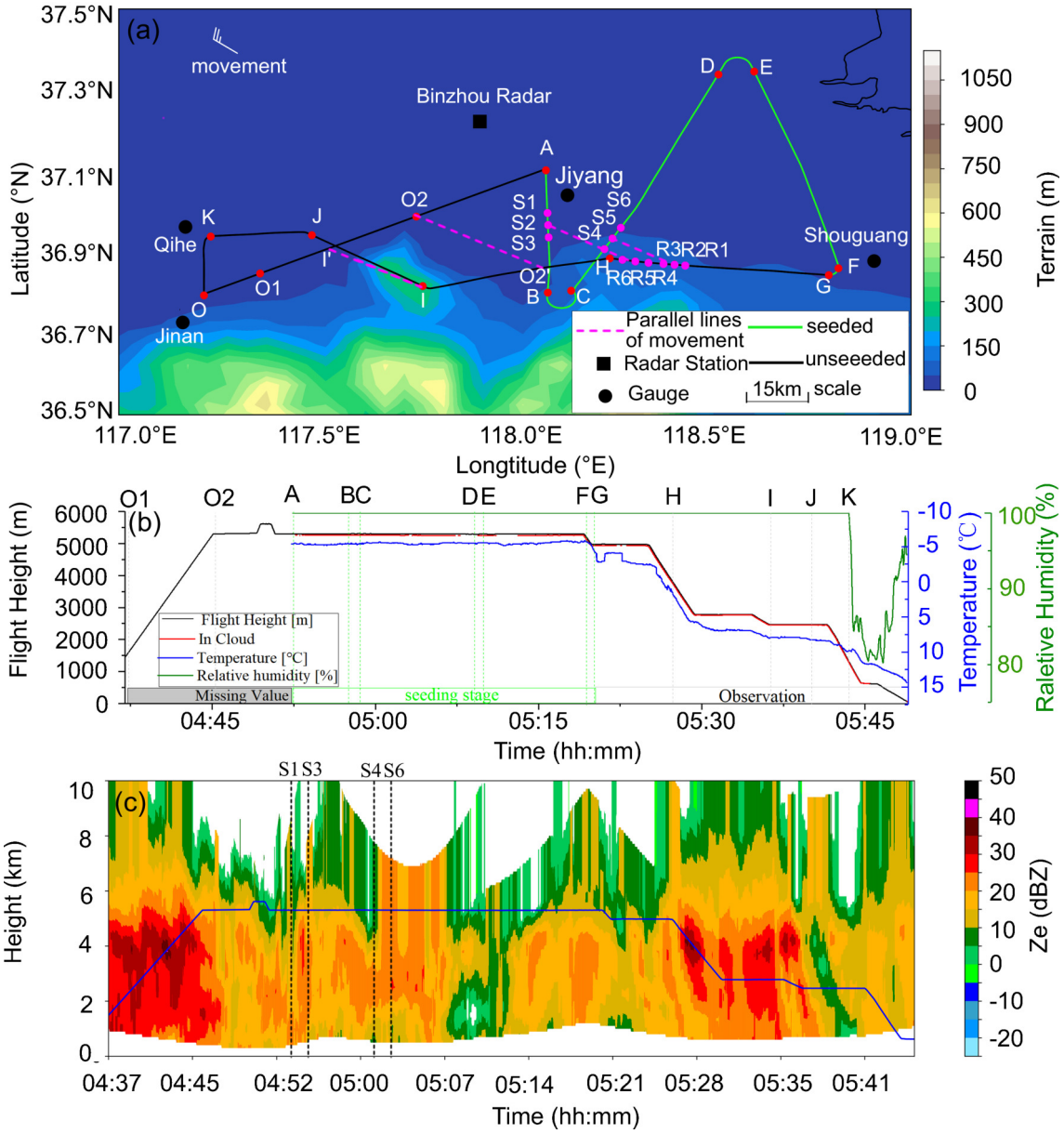

Fig. 3. (a) Regional DEM and the aircraft flight track from 0437 to 0549 UTC on 21 May 2018. The colored line is the flight track, the black box the location of Binzhou radar, and the letters A–I and red points the flight turning points. Note that the magenta lines represent the parallel lines of system movement with winds for the period between forward and backward flight time. (b) The characteristics of flight height (black line), in-cloud (red dot), flight speed (light blue), temperature (blue lines), relative humidity (green line) parameters from 0437 to 0549 UTC. (c) Vertical cross-section of radar reflectivity along the aircraft flight track from 0437 to 0549 UTC measured by the ground radar at Binzhou. The blue line is the flight track.

UTC) and R1–R3 (0524:25–0525:25 UTC), respectively. Note that the magenta lines represent the parallel lines of system movement with winds for the period between forward and backward flight time.

The cloud macro-physical characteristics during the seeding operation were obtained 0–2 km above the cloud top. The temperature was between −5°C and −8°C, and the relative humidity was uniformly at ~100% (Fig. 3b). Note that at 0437 UTC, moderate-intensity turbulence occurred. The aircraft experienced light, moderate, and then severe icing, indicating that the supercooled water content varied along the flight track.

Figure 3c shows the cross-section of radar reflectivity along the aircraft flight track from 0437 to 0549 UTC measured by the ground radar at Binzhou. Section A–B (seen from Fig. 3b) of the zigzag flight track was mostly covered with convective clouds, with convective centers at the height of 3–5 km and echo centers reaching above 30 dBZ at limited locations that are not clearly shown in Fig. 3c. Section C–D (seen from Fig. 3b) of the zigzag flight track was mostly covered with stratiform clouds with radar echoes below 25 dBZ. In addition, convection was observed during period S1–S3 (within A–B), while more stratiform clouds were observed during period S4–S6 (within C–D) (Fig. 3c).

4. Analysis and Results

4.1. *Evolving characteristics of airborne KPR echoes*

During the two seeding periods of S1–S3 and S4–S6 as well as the corresponding backward detection periods of R4–R6 and R1–R3 (Fig. 3a), the evolving characteristics of the real-time radar echoes by the airborne KPR were analyzed (Fig. 4). From Figs. 3c and 4c, it can be seen that the mixed convective-stratiform cloud is the target object for seeding operation. The convective region and the stratiform region in the mixed convective-stratiform clouds were selected for the seeding during S1–S3 and S4–S6, respectively. In addition, a bright band (temperature around 0°C) can be found within the height of 4200–4300 m. By comparing Figs. 4a and 4b, it can be found that during S1–S3 the radar echoes in the convective region were stronger after the seeding. An echo center of 20–35 dBZ appeared at the height of 2–4 km, and the echo top became dense and was uplifted by 0.5–1.0 km. The differences between Figs. 4d and 4e show that the echoes became significantly weaker above the seeding layer (5200 m) after the seeding operation in the stratiform region during S4–S6, and a hollow structure of echoes appeared at the height of 6.2–7.8 km, with the largest depth reaching

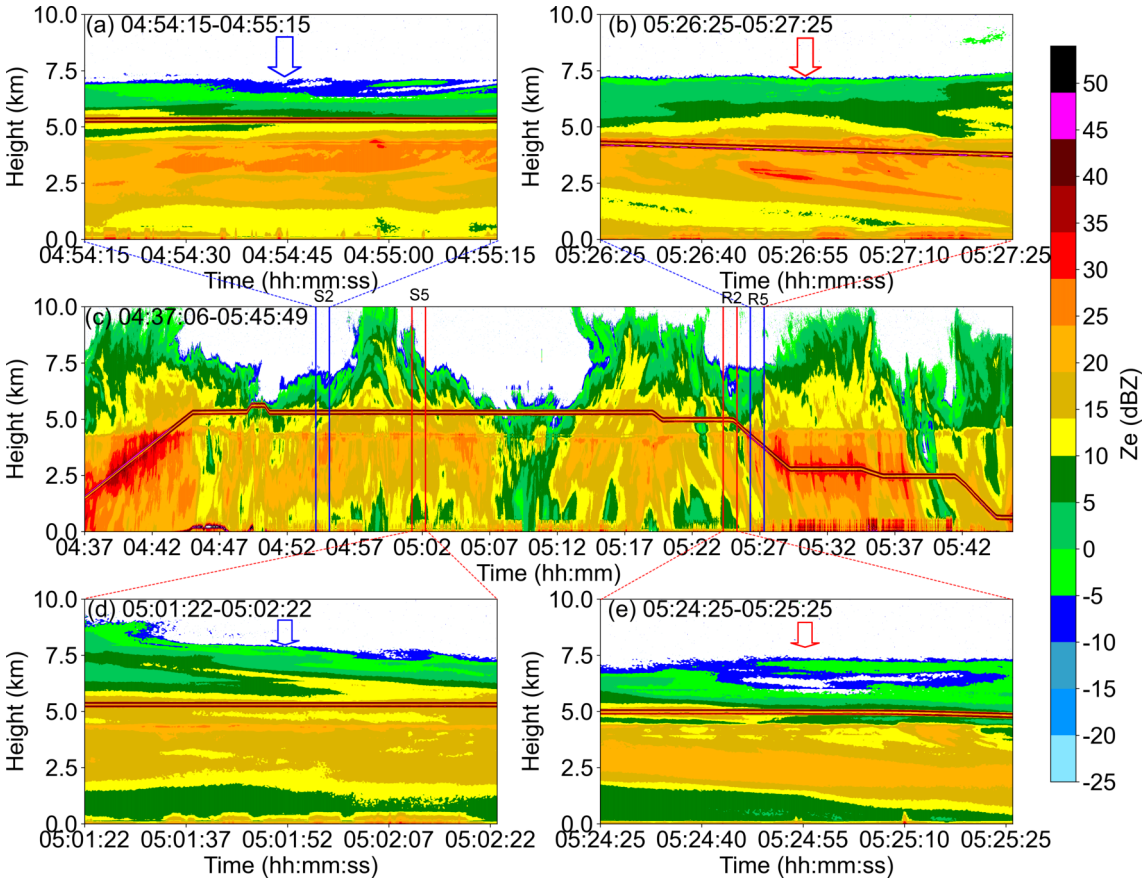

Fig. 4. Evolving characteristics of real-time airborne KPR radar echoes during (a) S1–S3, (b) R4–R6 (30–32 minutes after the seeding in S1–S3), (c) the whole detection period, (d) S4–S6, and (e) R1–R3 (22–24 minutes after the seeding in S4–S6). The positions pointed by the blue arrows are points S2 and S5 before the seeding operation, and the positions pointed by the red arrows are the points R5 and R2 after the seeding operation.

about 1.6 km and a diameter of about 5.5 km (calculated as follows: 0524:30–0525:20 UTC→50 s × 110 m s^{-1} = 5.5 km). The mechanism by which the hollow structure forms will be discussed in section 5. In addition, the top of the hollow part was covered by a thin layer with echoes being −5 dBZ (Fig. 4e). By comparing Figs. 4a and 4b as well as Figs. 4d and 4e, it is evident that the echoes were significantly enhanced at the height of 2–4 km 22–32 minutes after the seeding operation, with the enhancement amplitude exceeding 5 dBZ in all areas. In addition, a strong echo center of 35 dBZ appeared in the convective region.

Figure 5 shows the contoured frequency by altitude diagrams (CFADs) of the radar reflectivity Z_e for the two seeding periods. The CFADs explain the joint probability distribution function of height and reflectivity and represent the frequency distribution in a coordinate system of reflectivity bins (*x*-axis) and altitude (*y*-axis). In each CFAD, the distribution was normalized by dividing the observed frequency by the maximum frequency for all height-reflectivity bins, to compare the CFADs among different cases. During S1–S3, the differences of the echoes in the convective region prior to and after the seeding show that the echoes became stronger within a denser layer at heights of ~3 km surrounding the seeding layer, and that the echo top height increased by 1–2 km. In addition, the median Z_e was 5–7 dBZ larger than that before the seeding operation, and the echo near the surface increased to 28 dBZ from 12 dBZ (Figs. 5a and 5b). In contrast, Figs. 5c and 5d show that the echoes in the stratiform region became significantly weaker at heights of 2–3 km surrounding the seeding layer after the seeding during S4–S6. In addition, the median Z_e was 2–3 dBZ lower than that before the seeding, and the echo top height decreased by 1.4–1.7 km. Before the seeding operation, the median Ze reached the peak of 21.2 dBZ at the height of 3.5 km, and the Z_e decreased above and below this level, falling to 9 dBZ at the surface. During the period R1–R3, the variation trend of the Z_e median value was similar to that before the seeding. However, the peak Z_e value of 19.7 dBZ appeared at about 2.1 km, and Z_e was about 8.5 dBZ near the surface, which were both smaller than those before the seeding. We would like to mention that natural evolution could also play some roles to the variation of cloud properties indicated here and other places over seeded area, which are difficult to separate and further discussed later in the discussion section.

Figure 6 shows the CFADs of the Doppler radar velocity, with the same analysis method as shown in Fig. 5. The range of Doppler radar velocity widens after the seeding. Specifically, the velocity changes from 3–5 m s^{-1} to 5–8 m s^{-1} in the convective region, and from 3–5 m s^{-1} to 4–7 m s^{-1} in the stratiform region. Besides, the median, 25th and 75th percentiles of the Doppler radar velocity are very

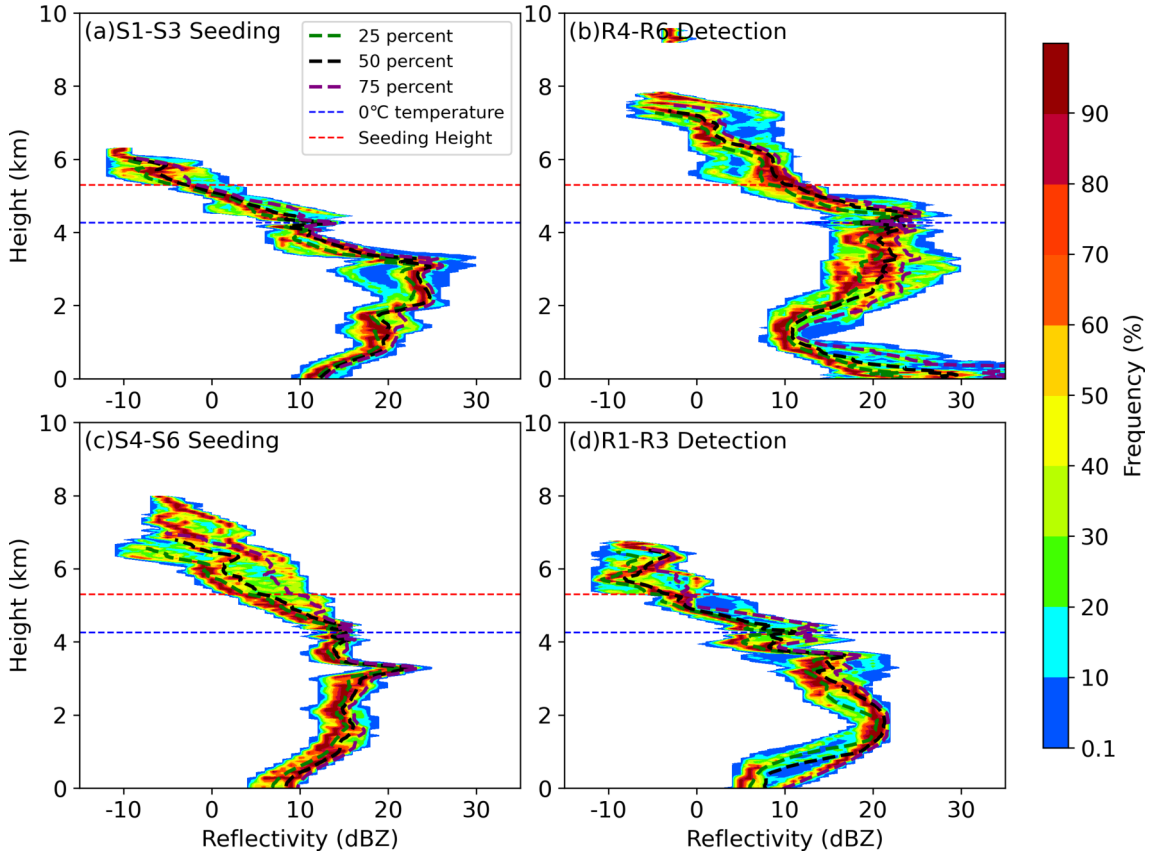

Fig. 5. Evolution of the CFADs of the radar reflectivity factors during (a) S1–S3, (b) R4–R6, (c) S4–S6 and (d) R1–R3. Green, black and purple dashed lines represent the 25th percentile, median and 75th percentile, respectively. The blue dashed line represents the freezing level and the red dashed line represents the seeding level.

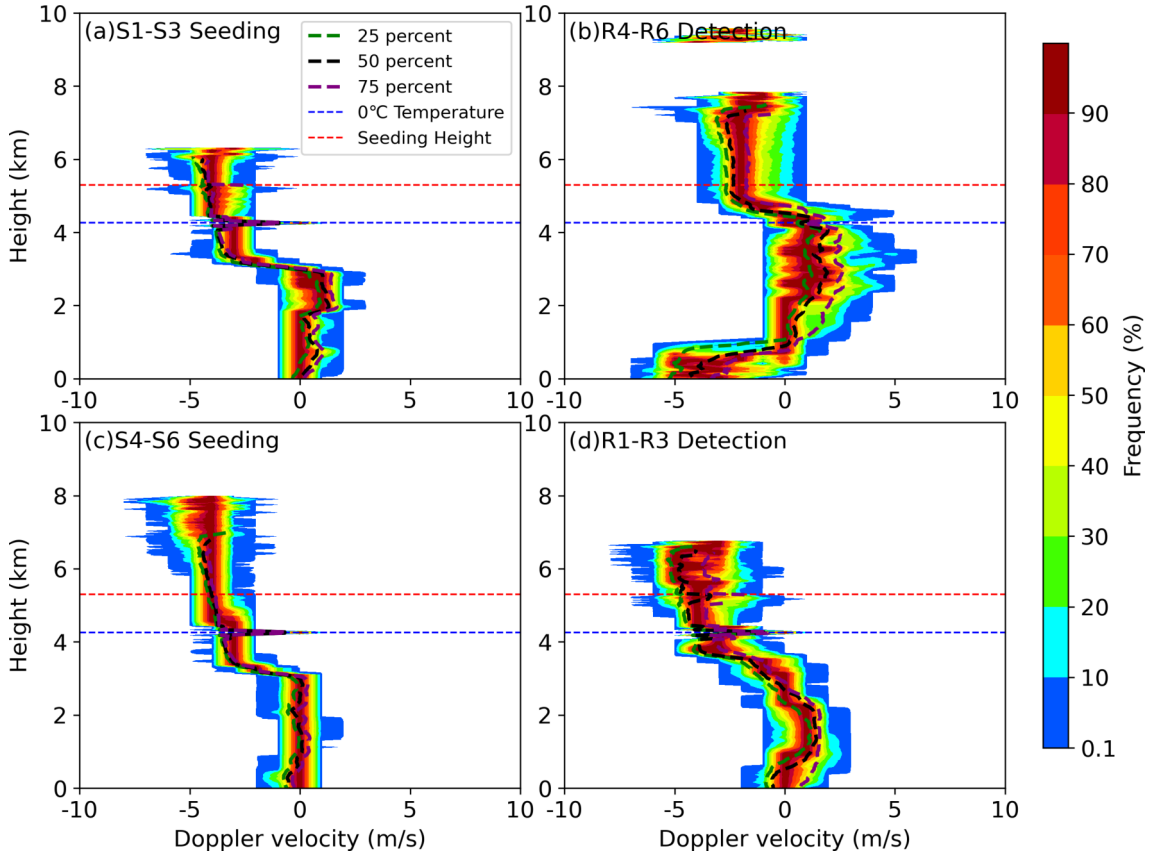

Fig. 6. Same as Fig. 5, but for the Doppler radar velocity. Positive velocity indicates downward motion and negative velocity indicates upward motion.

close to each other before the seeding, but after the seeding, the intervals between them distinctly increase. This implies that the microphysical processes play a role. After the seeding operation, the AgI was rapidly nucleated. In addition, in the environment with relatively abundant supercooled water, the Bergeron and collision-coalescence processes were accelerated, which favors the formation of large-size precipitation particles. Therefore, the particle spectrum was broadened, leading to different fall velocities of particles and a significant broadening of the velocity spectrum. As for the CFADs of Doppler radar velocity, there was a broadening of the overall Doppler radar velocity range and a significant increase in the terminal velocities of precipitation particles. About 30 minutes after the seeding in the convective region, the median terminal velocity increases from 0.5 m s^{-1} to 5.0 m s^{-1} in the convective region and from 1.0 m s^{-1} to 1.25 m s^{-1} in the stratiform region.

4.2. *Analysis of cloud microphysical properties from aircraft observations*

The above analysis of airborne KPR data shows that the seeding operation over different parts of the mixed convective-stratiform clouds leads to different evolutions of cloud macro-physical characteristics. In this section, we focus on the evolutions of microphysical characteristics after seeding in the convective and stratiform parts of cloud. However, we should note that the aircraft did not pass through the convective core partly for safety consideration. Instead, it went through the upper part of the convective region and made the measurements of cloud microphysical properties there. This would result in relatively low liquid water content and small droplet number concentration over the convective region. Thus, the analysis here mainly focuses on the evolution of microphysical characteristics after seeding over two regions, rather than their comparisons.

As shown in Figs. 7a–c, before the seeding, the convective cloud during S1–S3 and the stratiform cloud during S4–S6 were mainly composed of supercooled droplets. Specifically, the average diameter from the CDP was 7.4 μm during the period S1–S3, and the liquid water content (LWC) was 0.04 g m^{-3}, with a concentration of 25.5 cm^{-3}. During S4–S6, the average diameter from the CDP was 7.5 μm, and the LWC was 0.09 g m^{-3}, with a concentration of 79.6 cm^{-3}. The CIP concentrations were lower in both cloud regions, and the ice water contents (IWC) were also lower (4.0×10^{-6} and 5.7×10^{-5} g m^{-3}, respectively). The diameters of graupel particles and dendritic snow crystals in the stratiform cloud were larger than those in the convective cloud. After the seeding operation, the mean concentration, diameter and LWC from the CDP in both regions decreased significantly. In contrast, the mean concentration and diameter from the CIP and the IWC increased significantly. Therefore, snow crystals and droplets with diameters above 300 μm appeared, and the PIP concentration also increased by one order of mag-

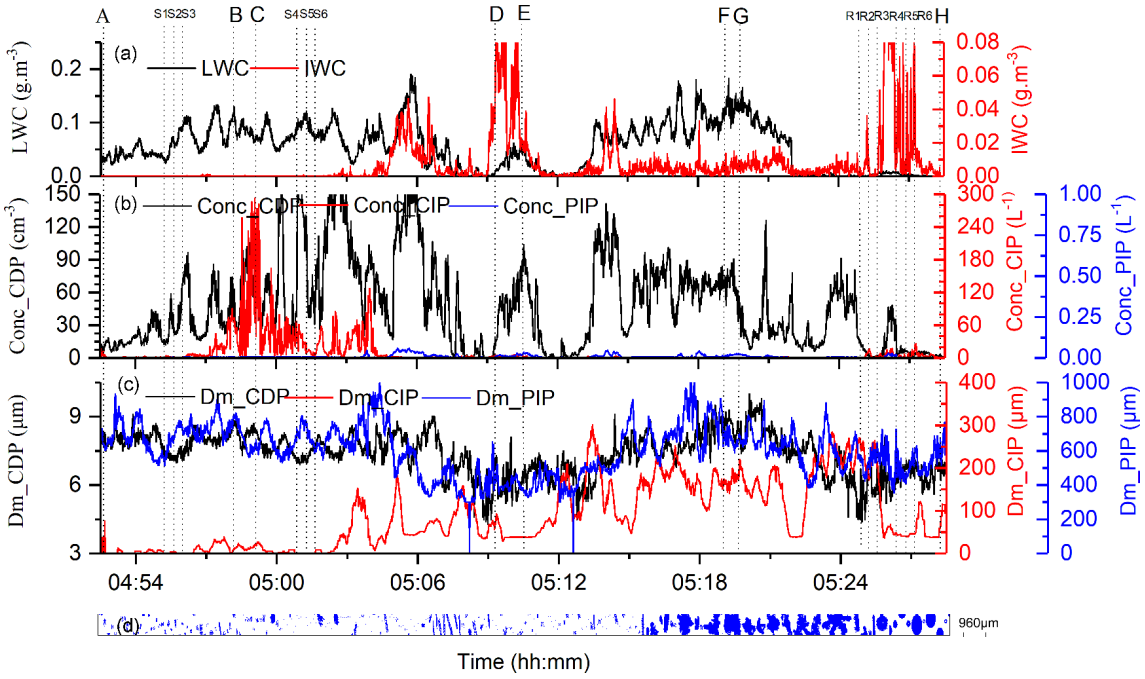

Fig. 7. Evolution of each microphysical variable at different operational times during the horizontal flight stage at 0452:30–0528:30 UTC. (a) LWC and IWC. (b) CDP, CIP, and PIP measured cloud particle concentration. (c) the particle size from CDP, CIP, and PIP. (d) CIP measured cloud particle image.

nitude. The CIP in Fig. 7d shows that the cloud was mainly composed of graupel particles and columnar ice crystals before the seeding, whereas after the seeding, there was a gas-phase riming process on the ice crystal surface that formed dendritic snow crystals, causing the coexistence of ice crystals and rimed snow crystals.

For the convective cloud during S1–S3, Fig. 8 shows that the mean concentrations from the CDP, CIP and PIP changed from 212.8 L^{-1} μm^{-1}, 0.017 L^{-1} μm^{-1} and 1.04×10^{-6} L^{-1} μm^{-1} to 139.2 L^{-1} μm^{-1}, 0.005 L^{-1} μm^{-1} and 1.64×10^{-4} L^{-1} μm^{-1} after the seeding operation, respectively. The particle size from the CDP peaked at 5.5 μm both before and after the seeding; and the size of large-size cloud particles, i.e., the particle size recorded by the CIP, increased with maximum value changing from 225 μm to 1250 μm after the seeding. Moreover, the maximum precipitation particle size increased from 400 μm to maximum measurable size, 6200 μm. For the stratiform cloud during S4–S6, the mean concentrations from the CDP, CIP and PIP changed from 561.7 L^{-1} μm^{-1}, 0.09 L^{-1} μm^{-1} and 1.0×10^{-8} L^{-1} μm^{-1} to 210.5 L^{-1} μm^{-1}, 0.05 L^{-1} μm^{-1} and 3.57×10^{-4} L^{-1} μm^{-1} after the seeding, respectively. In addition, the maximum precipitation particle size increased from 700 μm to 5700 μm. The concentrations from the CDP and CIP decreased significantly after two seeding operations. However, the PIP concentration increased by 2–4 orders of magnitude, and its maximum particle size increased by 8–15 times. Together with Fig. 7d, it can be inferred that deposition processes formed dendritic snow crystals on the surface of ice crystals. This suggests that after seeding with AgI, the transformation of water from liquid to ice phase was accelerated, and the transformation was quite efficient. Note that the aircraft observation locations during S1–S3 are about 1–2 km above the convective core, which cannot represent the convective cloud properties reliably, thus the differences in cloud microphysical properties measured by aircraft between regions S1–S3 and S4–S6 cannot indicate anything about cloud response differences between convective and stratiform parts. Instead, as indicated earlier, the information from aircraft is mainly used for investigation of temporal evolution of cloud properties by seeding. The differences between Figs. 6a and 6b show that the upward Doppler velocity at the height of 1.0–4.5 km in the convective cloud increased from 0–0.5 m s^{-1} to 3–5 m s^{-1}. The larger upward velocity favors the upward transport and condensation of water vapor. During this process, updrafts could also carry the AgI to higher levels where there is lower temperature, greater supersaturation and greater supercooled water content. Note that the latent heat released by the deposition of supercooled water enhances the convective cloud development further because this heat release can lead to stronger updrafts and higher cloud tops. These factors accelerate the Bergeron and collision-coalescence processes to form large-size precipitation particles after seeding of the AgI, thereby increasing the precipitation (Simpson and Woodley, 1971; Sax et al., 1979; Woodley et al., 1982; Rosenfeld and Woodley, 1989; Bruintjes, 1999).

4.3. *Evolution of seeding-producing ice monitored by satellites*

(1) Analysis of NPP observations

To analyze the characteristics of the microphysical struc-

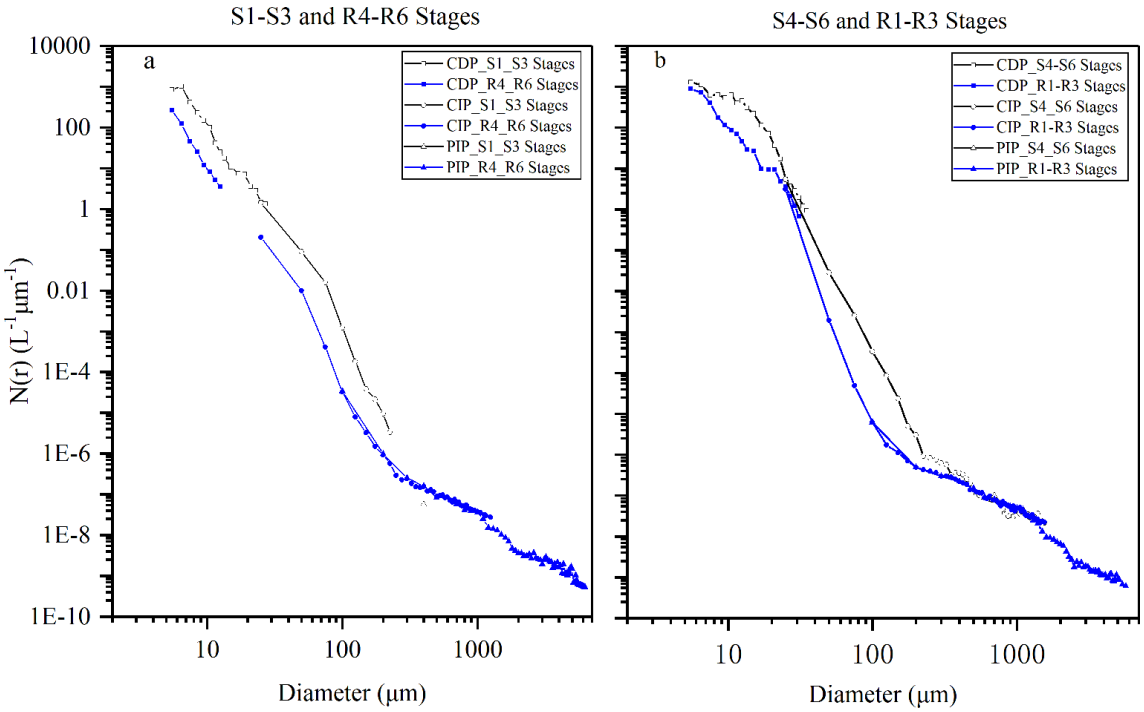

Fig. 8. Cloud particle size spectra during (a) S1–S3 and R4–R6 in convective cloud, and during (b) S4–S6 and R1–R3 in stratiform cloud. The black line segments are the measurements during the seeding operation, and the blue segments during the detection period. The squares denote data from the CDP, from the CIP and triangles from the PIP.

ture of cloud tracks in detail, the high resolution data from the NPP/Visible Infrared Imaging Radiometer Suite sensor at 0525 UTC on 21 May 2018 were processed based on microphysical principles (Figs. 9a–b). The flight tracks are colored in green, superimposed on the surrounding supercooled water cloud which was shaded in yellow and orange. Figs. 9a–b show evidence of a "cloud seeding track" (referred to as the cloud track) on the cloud top near the dashed line in Fig. 9c, which is almost parallel to the section C–D in the flight track, with the cloud track extended about 15 km away from point C. Actually, the dashed line in Fig. 9c is near to the location where section C–D was translated after 28–7 minutes of cloud seeding as the satellite passed by. The visible channel in Fig. 9b shows a southwest-northeast oriented seeding track 15–20 km southeast of section C–D, which indicates that the supercooled water in the cloud was at least partially glaciated into ice particles; thus, as the cloud particles became larger and sank, this lowering the cloud top. In Fig. 9a, the shallow depth in cross-section 4 and the almost zero depth in cross-section 2 may be caused by the veiling of newly formed thin supercooled water cloud with small particle size. Figure. 9c shows that the section C–D, which had translated along the wind direction of 300° at a speed of 11 m s^{-1} for 7–28 minutes from the original positions, was just inside the cloud track during 0458:42–0509:04 UTC. This result is consistent with the above analysis. Moreover, the brightness temperature (TBB) during the period R1–R3 was significantly higher than that during the period R4–R6, indicating the strong convective activity in the convective cloud region.

(2) Analysis of the H8 satellite data

To track the evolution and movement of the cloud tops after the seeding operation, the high-resolution data from the H8 satellite were adopted for further examination. The 10-minute TBB from the 12 μm channel on the H8 satellite (Fig. 10) shows that the convective clouds in section A–B became blocky after the seeding operation during 0452–0457 UTC, and the TBB gradually decreased (note that seeded "A–B section" moves downwind with time), indicating the stronger convective activity. The stratiform cloud in section C–D for seeding operation was located in front of a large block of mixed convective-stratiform clouds during 0458–0509 UTC. About 15 minutes after the seeding, a seeding track with a width of 1–3 km appeared 10 km downstream of the seeding layer. After another 7 minutes, a cloud seeding track with a width of 3–5 km appeared at locations about 15–20 km downstream of the seeding layer and continued to drift southeastward at 11 m s^{-1} along the wind direction of 300°. By 0550 UTC, the seeding track had already moved out of the flight area. Moreover, the seeding track below section G–H became narrow after its formation, which is likely due to the diffusion of the water cloud near the seeded volume to the cloud track center. It is also likely associated with the coverage of the newly-formed thin super-cooled water cloud with quite small particle size.

To examine the evolving trend of the cloud seeding tracks more clearly, the downstream trajectory of section C–D computed at 10-minute intervals along the wind direc-

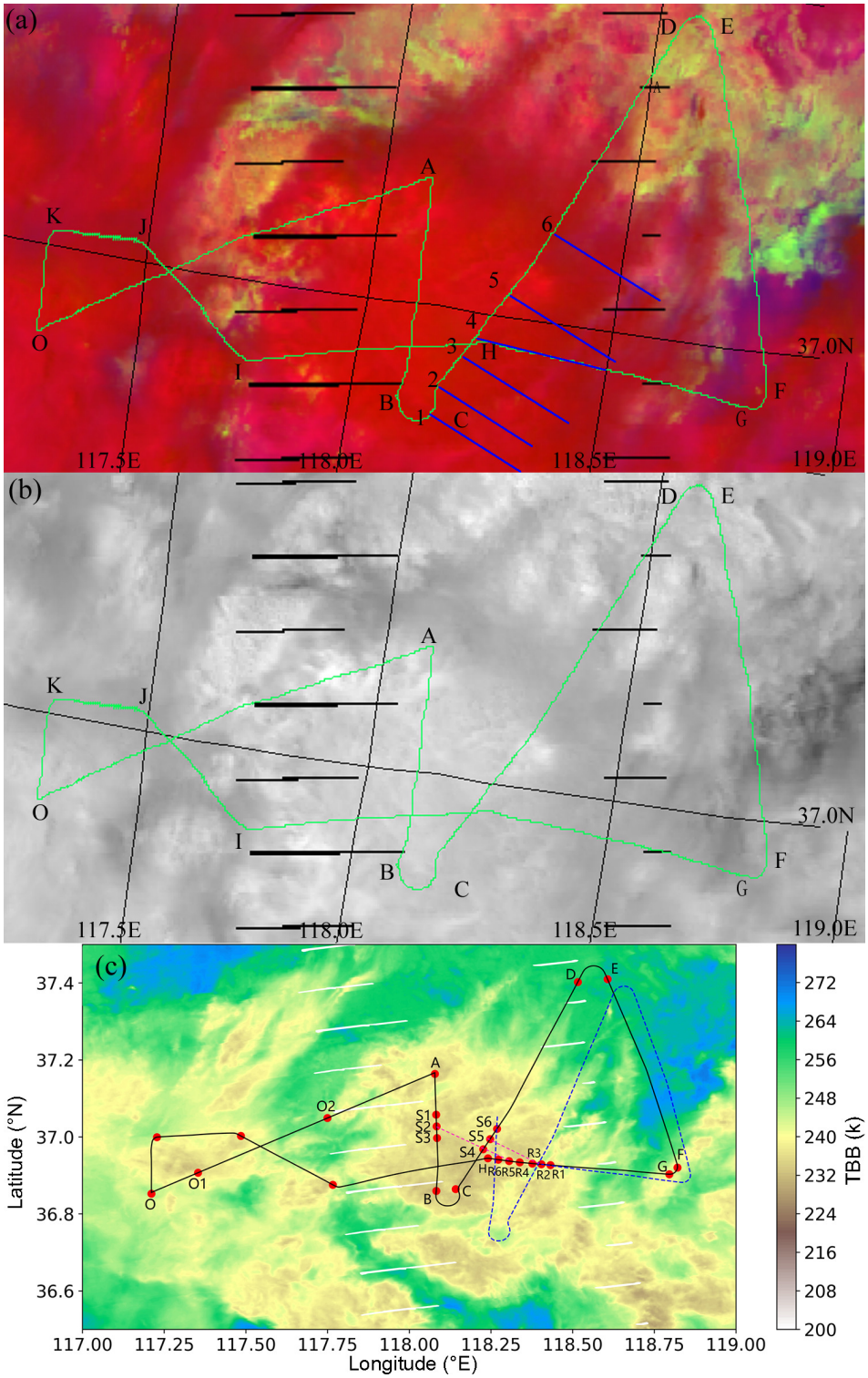

Fig. 9. S-NPP VIIRS microphysical seeding track over eastern China at 0525 UTC on 21 May 2018. The aircraft flew eastward so that the seeding track becomes older from right to left. (a) Red color composite is the visible reflectance, green for the 3.7 μm reflectance, and blue for the 10.8 μm brightness temperature. Note that the six blue lines except the one labeled with "4" represent the moving tracks of cloud parts seeded (at location 1–6 except 4) with winds; and the blue line labeled with "4" represents the flight track in which aircraft measured the response of cloud properties after seeding for locations between 4 and 5 and between A and B (such as S1–S6 as shown in panel c). (b) 0.6 μm reflectance. (c) TBB from the12-μm channel with black lines showing the flight track and blue dotted lines for the flight track translated along the wind direction of 300° after 7–28 minutes from the original position A–H.

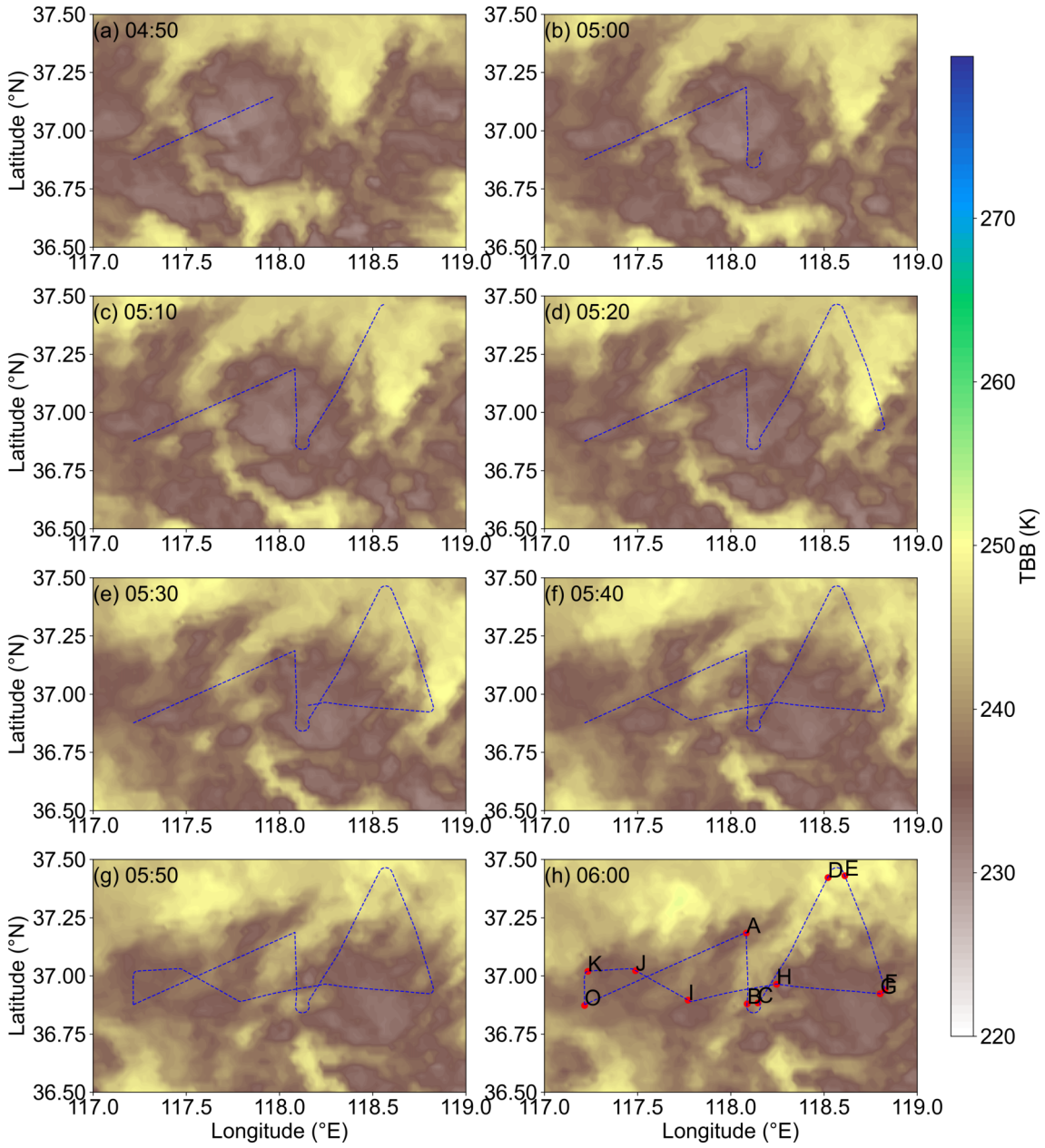

Fig. 10. Evolving cloud characteristics from the 10-minute TBB at 12-μm channel on the H8 satellite from 0450–0600 UTC. Blue dashed lines are the actual flight track, and letters A–K are turning points.

tion of 300° at 11 m s^{-1} was calculated. Then, the TBB values at 12-μm channel from the H8 satellite for each moving trajectory were extracted, and the boxplot of the TBB values was further obtained, as shown in Fig. 11. The 50th percentile of the TBB values shows a gradually increasing trend with time with a linear fitting line of TBB = $0.5068\Delta T + 234.87$, where ΔT is the number of time intervals from 0500 UTC with the interval being 10 minutes. Note that the correlation coefficient between the 50th percentile of TBB and ΔT was 0.87. The TBB had increased by 4.1 K until 0600 UTC, which indicates that the seeding track became more and more obvious, along with significant increases in its width and depth. Besides, the TBB decreased slightly at 0540 UTC, which was likely attributed to the coverage of the newly-formed thin super-cooled water cloud. This result was consistent with the conclusions above.

5. Conceptual model for seeding operations of the mixed convective-stratiform clouds

Based on the above analysis results, a conceptual model of the AgI seeding for mixed convective-stratiform clouds is proposed, as shown in Fig. 12. Before the seeding operation (Fig. 12a), there are few ice crystals but many small cloud droplets in both the convective and stratiform parts of the cloud. In addition, there is a strong updraft in the convective region, resulting in the appearance of a convective core.

After the seeding of AgI (Fig. 12b), the ice crystals, snow crystals and precipitation particles rapidly increase in both parts. Moreover, due to the potential dynamic seeding mechanisms, enhanced updraft appears near the convective core, leading to a significant enhancement of convection.

The model shows distinct responses of different parts of the mixed convective-stratiform clouds to the seeding operation. Specifically, the convective region displays more vigorous convective activity after the seeding operation, with significantly enhanced echoes and higher echo tops. In addition, the dynamic seeding mechanism may also be involved, favoring the growth of particle size and broader full-spectra. The concentration of precipitation particles is higher and thus more precipitation forms. In contrast, after the seeding of AgI in the stratiform region, the transformation between droplets and ice crystals is accelerated, causing the surrounding supercooled water to condense into ice crystals. Subsequently, the ice crystals develop and fall under the effects of the Bergeron and collision-coalescence processes. At that time, the echoes significantly weaken at heights within 2–3

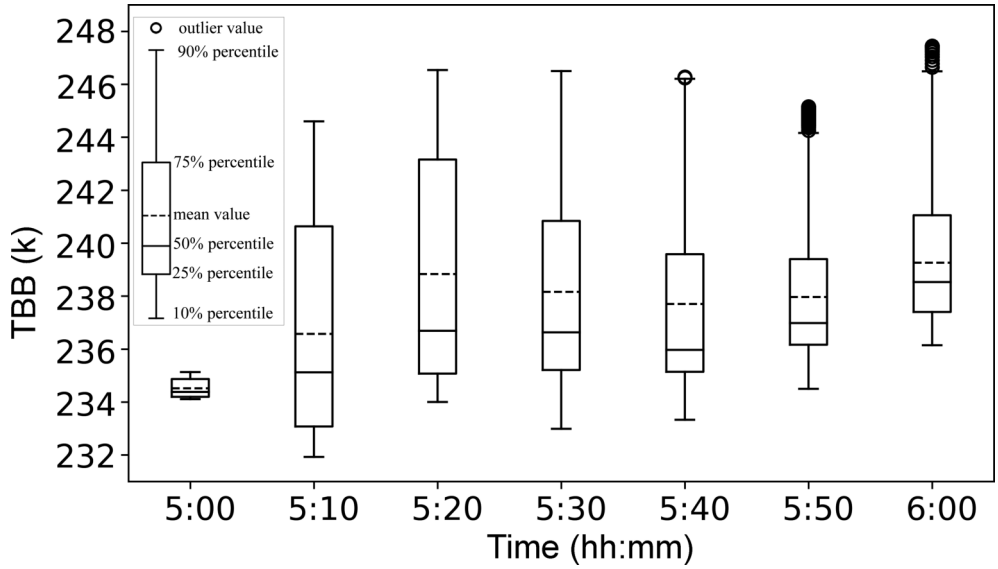

Fig. 11. Evolving characteristics of the 10-minute TBB at 12 μm channel on the H8 satellite extracted along the moving section C–D. The solid line inside the box represents the 50th percentile, the lower line the 25th percentile, the upper line the 75th percentile, the dotted line the mean value, and the lower and upper whiskers denote the 10th and 90th percentiles, respectively.

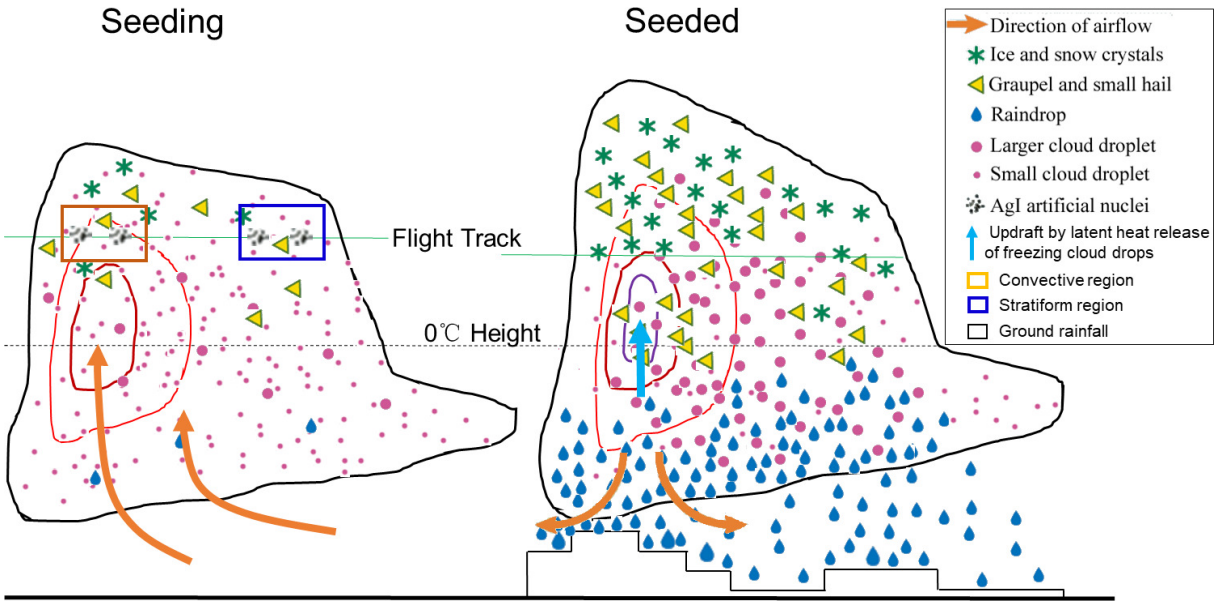

Fig. 12. Conceptual model of seeding AgI over different parts of the mixed convective-stratiform clouds. The left panel shows the situation before seeding, and the right panel shows that after seeding. Green solid line denotes the flight track, and black dashed line the freezing level. Signs such as particle category and airflow are shown in the legend.

km around the seeding layer, the echo top lowers, and obvious icing seeding tracks with a hollow structure appear. Eventually, large-size particles fall to the ground as surface precipitation. In this process, the static seeding mechanism plays the crucial role.

6. Conclusion and discussion

In this study, based on observations from the airborne KPR, NPP satellite and high-resolution H8 satellite, the cloud macro- and micro-physical characteristics as well as responses to the seeding operation in the convective and stratiform regions for a mixed convective-stratiform cloud occurred in Shandong during spring were analyzed. The main conclusions are as follows.

Based on the in-situ aircraft (equipped with the KPR) observations, different physical responses to the seeding in the convective and stratiform regions of the mixed convective-stratiform clouds were tracked and investigated. In terms of the convective region, the radar echoes became stronger with a denser depth, and the echo top height increased by 0.5–1.0 km. The median Z_e was 5–7 dBZ higher than that before the seeding, and the near-surface Z_e increased to 28 dBZ from 12 dBZ. The concentrations from the CDP and CIP both decreased significantly. However, the PIP concentration increased by 2–4 orders of magnitude, and the maximum size of precipitation particles increased from 400 μm to 6200 μm, i.e., by a factor of more than 15. This implies that the AgI seeding in the convective region accelerated the formation of large-size precipitation particles by the Bergeron, riming and collision-coalescence processes. In the stratiform region, there were obvious icing seeding tracks after the seeding operation. The echoes became significantly weaker at heights within about 2–3 km around the seeding layer, and the echo top height was lowered by 1.4–1.7 km. The median Z_e was 2–3 dBZ lower than that before the seeding. In addition, a hollow structure of the echoes appeared within the height of 6.2–7.8 km, with the largest depth reaching about 1.6 km, a diameter of about 5.5 km and a duration of 1 hour. The size of precipitation particles increased from 700 μm to 5700 μm, thus by a factor of more than 8. Moreover, gas-phase riming processes helped form dendritic snow crystals on the surface of ice crystals, causing the coexistence of ice crystals and rimed snow crystals. This phenomenon indicates that after seeding the AgI, the transformation between cloud and water was accelerated, which was quite complete and efficient.

The tracking and monitoring by the NPP and H8 satellites showed that the convective clouds became blocky after the seeding. In addition, the TBB decreased, indicating stronger convective activity in the convective region. In addition, 15 minutes after seeding the AgI in the stratiform region, a cloud seeding track with a width of 1–3 km appeared 10 km downstream of the seeding layer. Approximately 7 minutes later, a cloud seeding track with a width of 3–5 km appeared 15 km downstream of the seeding layer and drifted southeastward at a speed of 11 m s^{-1} along the wind direction of 300° for 1 hour.

Comparing the physical responses to the seeding in two regions, it is found that in the convective region there were significant upward Doppler radar velocities of 3–5 m s^{-1} at the heights of 1.0–4.5 km, which are favorable for the upward transport and further condensation of the water vapor. Moreover, the updrafts of convective clouds may also carry the AgI to higher levels where there is lower temperature, higher supersaturation and higher supercooled water content. Note that the latent heat released by the condensation of supercooled water should enhance the effect of seeding on the convective cloud further, because this heat release can lead to stronger updrafts and higher cloud tops. These factors may result in the formation of large-size precipitation particles by accelerating the effects of Bergeron and collision-coalescence processes after seeding the AgI, thereby increasing the precipitation. However, in the stratiform region, the static seeding mechanism played the dominant role. That is, the surrounding supercooled water condensed into ice crystals by seeding the AgI, and then through the deposition process the ice crystals grew and fell onto the ground as surface precipitation.

A challenging question we should note is the relative contributions of cloud seeding versus natural variability to the observed phenomenon after cloud seeding. In principle, it is almost impossible to answer from a purely observational view since we do not have two identical clouds to compare with and without cloud seeding. Thus, we here have simply attributed the cloud property changes mostly to cloud seeding, which warrants further investigation in the future with mesoscale weather model simulations.

Acknowledgements. This work was supported by the National Key Research and Development Project (Grant No. 2019YFA0606803 and 2016YFA0601704), the National Natural Science Foundation of China (Grant No. 41925022), the Innovation and Development Project of China Meteorological Administration (CXFZ2022J036), and the Science and Technology Development Fund of Hubei Meteorological Bureau (Grant No. 2017Y06, 2017Y07, 2016Y06, and 2019Y10). NOAA Data Service Network provided NPP satellite data, the H8 10-minute full-disc data was also provided by the Data Service website of NOAA, and Binzhou Meteorological Observatory in Shandong Province provided valuable radar observation data and ground real-time data. In addition, we thank Nanjing Hurricane Translation for reviewing the English language quality of this paper.

Data Availability Statement The data used in this study are available at https://pan.baidu.com/s/1wwwCLKjTGy_HxDXdQFJd4Q.

REFERENCES

Biondini, R., J. Simpson, and W. Woodley, 1977: Empirical predictors for natural and seeded rainfall in the Florida area cumulus experiment (FACE), 1970–1975. *J. Appl. Meteorol.*, **16**, 585–594, https://doi.org/10.1175/1520-0450(1977)016<0585:EPFNAS>2.0.CO;2.

Boe, B. A., J. A. Heimbach Jr., T. W. Krauss, L. L. Xue, X. Chu, and J. T. McPartland, 2014: The dispersion of silver iodide particles from ground-based generators over complex terrain. Part I: Observations with acoustic ice nucleus counters. *J. Appl. Meteorol. Climatol.*, **53**, 1325–1341, https://doi.org/10.1175/JAMC-D-13-0240.1.

Bruintjes, R. T., 1999: A review of cloud seeding experiments to enhance precipitation and some new prospects. *Bull. Amer. Meteor. Soc.*, **80**, 805–820, https://doi.org/10.1175/1520-0477(1999)080<0805:AROCSE>2.0.CO;2.

Cai, Z. X., Y. Q. Zhou, and M. Cai, 2013: Analysis on comprehensive observation of artificial precipitation enhancement operation for a convective-stratiform mixed cloud. *Plateau Meteorology*, **32**(5), 1460–1469, https://doi.org/10.7522/j.issn.1000-0534.2012.00115. (in Chinese with English abstract)

DeMott, P. J., 1997: Report to North Dakota Atmospheric Resource Board and Weather Modification Incorporated on tests of the ice nucleating ability of aerosols produced by the Lohse Airborne Generator. Colorado State University Department of Atmospheric Science Tech. Rep., 38 pp.

Dong, X. B., C. F. Zhao, Y. Yang, Y. Wang, Y. Sun, and R. Fan, 2020: Distinct change of supercooled liquid cloud properties by aerosols from an aircraft - based seeding experiment. *Earth and Space Science*, **7**, e2020EA001196, https://doi.org/10.1029/2020EA001196.

French, J. R., and Coauthors, 2018: Precipitation formation from orographic cloud seeding. *Proceedings of the National Academy of Sciences of the United States of America*, **115**(6), 1168–1173, https://doi.org/10.1073/pnas.1716995115.

Gabriel, K. R., 1999: Ratio statistics for randomized experiments in precipitation stimulation. *J. Appl. Meteorol.*, **38**, 290–301, https://doi.org/10.1175/1520-0450(1999)038<0290:RSFREI>2.0.CO;2.

Hallet, J., 1981: Ice crystal evolution in Florida summer cumuli following AgI seeding. Preprints, Eighth Conference on Inadvertent and Planned Weather Modification, Reno, NV, Amer. Meteor. Soc., 114–115.

Heymsfield, A. J., G. Thompson, H. Morrison, A. Bansemer, R. M. Rasmussen, P. Minnis, Z. E. Wang, and D. M. Zhang, 2011: Formation and spread of aircraft-induced holes in clouds. *Science*, **333**, 77–81, https://doi.org/10.1126/science.1202851.

Heymsfield, G. M., L. Tian, L. H. Li, M. McLinden, and J. I. Cervantes, 2013: Airborne radar observations of severe hailstorms: Implications for future spaceborne radar. *J. Appl. Meteorol. Climatol.*, **52**, 1851–1867, https://doi.org/10.1175/JAMC-D-12-0144.1.

Hillger, D., and Coauthors, 2013: First-light imagery from Suomi NPP VIIRS. *Bull. Amer. Meteor. Soc.*, **94**(7), 1019–1029, https://doi.org/10.1175/BAMS-D-12-00097.1.

Hobbs, P. V., J. H. Lyons, J. D. Locatelli, K. R. Biswas, L. F. Radke, R. R. Weiss, and A. L. Rangno, 1981: Radar detection of cloud-seeding effects. *Science*, **213**, 1250–1252, https://doi.org/10.1126/science.213.4513.1250.

Jing, X. Q., and B. Geerts, 2015: Dual-polarization radar data analysis of the impact of ground-based glaciogenic seeding on winter orographic clouds. Part II: Convective clouds. *J. Appl. Meteorol. Climatol.*, **54**, 2099–2117, https://doi.org/10.1175/JAMC-D-15-0056.1.

Jing, X. Q., B. Geerts, K. Friedrich, and B. Pokharel, 2015: Dual-polarization radar data analysis of the impact of ground-based glaciogenic seeding on winter orographic clouds. Part I: Mostly stratiform clouds. *J. Appl. Meteorol. Climatol.*, **54**, 1944–1969, https://doi.org/10.1175/JAMC-D-14-0257.1.

Jing, X. Q., B. Geerts, and B. Boe, 2016: The extra-area effect of orographic cloud seeding: Observational evidence of precipitation enhancement downwind of the target mountain. *J. Appl. Meteorol. Climatol.*, **55**, 1409–1424, https://doi.org/10.1175/JAMC-D-15-0188.1.

Lance, S., 2012: Coincidence errors in a cloud droplet probe (CDP) and a cloud and aerosol spectrometer (CAS), and the improved performance of a modified CDP. *J. Atmos. Oceanic Technol.*, **29**(10), 1532–1541, https://doi.org/10.1175/JTECH-D-11-00208.1.

Langmuir, I., 1950: Control of precipitation from cumulus clouds by various seeding techniques. *Science*, **112**, 35–41, https://doi.org/10.1126/science.112.2898.35.

Lawson, R. P., B. Baker, B. Pilson, and Q. X. Mo, 2006: In situ observations of the microphysical properties of wave, cirrus, and anvil clouds. Part II: Cirrus clouds. *J. Atmos. Sci.*, **63**(12), 3186–3203, https://doi.org/10.1175/JAS3803.1.

Lawson, R. P., B. Pilson, B. Baker, Q. Mo, E. Jensen, L. Pfister, and P. Bui, 2008: Aircraft measurements of microphysical properties of subvisible cirrus in the tropical tropopause layer. *Atmospheric Chemistry and Physics*, **8**(6), 1609–1620, https://doi.org/10.5194/acp-8-1609-2008.

Lawson, R. P., S. Woods, and H. Morrison, 2015: The microphysics of ice and precipitation development in tropical cumulus clouds. *J. Atmos. Sci.*, **72**, 2429–2445, https://doi.org/10.1175/JAS-D-14-0274.1.

Lawson, R. P., and Coauthors, 2019: A review of ice particle shapes in cirrus formed in situ and in anvils. *J. Geophys. Res.: Atmos.*, **124**, 10 049–10 090, https://doi.org/10.1029/2018JD030122.

Lin, G., B. Geerts, Z. E. Wang, C. Grasmick, X. Q. Jing, and J. Yang, 2019: Interactions between a nocturnal MCS and the stable boundary layer as observed by an airborne compact Raman Lidar during PECAN. *Mon. Wea. Rev.*, **147**, 3169–3189, https://doi.org/10.1175/MWR-D-18-0388.1.

Nirel, R., and D. Rosenfeld, 1995: Estimation of the effect of operational seeding on rain amounts in Israel. *J. Appl. Meteorol.*, **34**, 2220–2229, https://doi.org/10.1175/1520-0450(1995)034<2220:EOTEOO>2.0.CO;2.

Orville, H. D., 1996: A review of cloud modeling in weather modification. *Bull. Amer. Meteor. Soc.*, **77**, 1535–1556, https://doi.org/10.1175/1520-0477(1996)077<1535:AROCMI>2.0.CO;2.

Pazmany, A. L., and S. J. Haimov, 2018: Coherent power measurements with a compact airborne Ka-band precipitation radar. *J. Atmos. Oceanic Technol.*, **35**, 3–20, https://doi.org/10.1175/JTECH-D-17-0058.1.

Pokharel, B., B. Geerts, and X. Q. Jing, 2015: The impact of ground-based glaciogenic seeding on clouds and precipitation over mountains: A case study of a shallow orographic cloud with large supercooled droplets. *J. Geophys. Res. Atmos.*, **120**, 6056–6079, https://doi.org/10.1002/2014JD022693.

Rosenfeld, D., and W. L. Woodley, 1989: Effects of cloud seeding in west Texas. *J. Appl. Meteorol.*, **28**, 1050–1080, https://doi.org/10.1175/1520-0450(1989)028<1050:EOCSIW>2.0.CO;2.

Rosenfeld, D., X. Yu, and J. Dai, 2005: Satellite-retrieved microstructure of AgI seeding tracks in supercooled layer clouds. *J. Appl. Meteorol.*, **44**, 760–767, https://doi.org/10.1175/JAM2225.1.

Rosenfeld, D., G. Liu, X. Yu, Y. Zhu, J. Dai, X. Xu, and Z. Yue, 2014: High-resolution (375m) cloud microstructure as seen from the NPP/VIIRS satellite imager. *Atmospheric Chemistry and Physics*, **14**(5), 2479–2496, https://doi.org/10.5194/acp-14-2479-2014.

Sax, R. I., J. Thomas, M. Bonebrake, and J. Hallett, 1979: Ice evolution within seeded and nonseeded Florida cumuli. *J. Appl. Meteorol.*, **18**, 203–214, https://doi.org/10.1175/1520-0450(1979)018<0203:IEWSAN>2.0.CO;2.

Silverman, B. A., 2001: A critical assessment of glaciogenic seeding of convective clouds for rainfall enhancement. *Bull. Amer. Meteor. Soc.*, **82**, 903–924, https://doi.org/10.1175/1520-0477(2001)082<0903:ACAOGS>2.3.CO;2.

Simpson, J., and W. L. Woodley, 1971: Seeding cumulus in Florida: New 1970 results. *Science*, **172**, 117–126, https://doi.org/10.1126/science.172.3979.117.

Smith, E. J., 1949: Experiments in seeding cumuliform cloud layers with dry ice. *Australian Journal of Scientific Research*, **2**, 78–91, https://doi.org/10.1071/CH9490078.

Vonnegut, B., and H. Chessin, 1971: Ice nucleation by coprecipitated silver iodide and silver bromide. *Science*, **174**, 945–946, https://doi.org/10.1126/science.174.4012.945.

Woodley, W. L., and D. Rosenfeld, 2004: The development and testing of a new method to evaluate the operational cloud-seeding programs in Texas. *J. Appl. Meteorol.*, **43**, 249–263, https://doi.org/10.1175/1520-0450(2004)043<0249:TDA-TOA>2.0.CO;2.

Woodley, W. L., J. Jordan, A. Barnston, J. Simpson, R. Biondini, and J. Flueck, 1982: Rainfall results of the Florida Area Cumulus Experiment, 1970–76. *J. Appl. Meteorol.*, **21**, 139–164, https://doi.org/10.1175/1520-0450(1982)021<0139:RROTFA>2.0.CO;2.

Woodley, W. L., D. Rosenfeld, and B. A. Silverman, 2003: Results of on-top glaciogenic cloud seeding in Thailand. Part I: The demonstration experiment. *J. Appl. Meteorol.*, **42**, 920–938, https://doi.org/10.1175/1520-0450(2003)042<0920:ROOGCS>2.0.CO;2.

Xue, L. L., and Coauthors, 2013a: Implementation of a silver iodide cloud-seeding parameterization in WRF. Part I: Model description and idealized 2D sensitivity tests. *J. Appl. Meteorol. Climatol.*, **52**, 1433–1457, https://doi.org/10.1175/JAMC-D-12-0148.1.

Xue, L. L., S. A. Tessendorf, E. Nelson, R. Rasmussen, D. Breed, S. Parkinson, P. Holbrook, and D. Blestrud, 2013b: Implementation of a silver iodide cloud-seeding parameterization in WRF. Part II: 3D simulations of actual seeding events and sensitivity tests. *J. Appl. Meteorol. Climatol.*, **52**, 1458–1476, https://doi.org/10.1175/JAMC-D-12-0149.1.

Xue, L. L., X. Chu, R. Rasmussen, D. Breed, B. Boe, and B. Greets, 2014: The dispersion of silver iodide particles from ground-based generators over complex terrain. Part II: WRF large-eddy simulations versus observations. *J. Appl. Meteorol. Climatol.*, **53**, 1342–1361, https://doi.org/10.1175/JAMC-D-13-0241.1.

Yang, J. M., and Coauthors, 2020: Spatial distribution and impacts of aerosols on clouds under Meiyu frontal weather background over central China based on aircraft observations. *J. Geophys. Res.: Atmos.*, **125**, e2019JD031915, https://doi.org/10.1029/2019JD031915.

Yang, Y., and Coauthors, 2019: Toward understanding the process-level impacts of aerosols on microphysical properties of shallow cumulus cloud using aircraft observations. *Atmospheric Research*, **221**, 27–33, https://doi.org/10.1016/j.atmosres.2019.01.027.

Zhao, C. F., L. J. Zhao, and X. B. Dong, 2019: A case study of stratus cloud properties using in situ aircraft observations over Huanghua, China. *Atmosphere*, **10**(1), 19, https://doi.org/10.3390/atmos10010019.